Investigation of Analytical Models for Surface-Mounted Permanent Magnet Motor Using Voltage Source Inverter

Zhaokai Li, Xiaoyan Huang, *Member, IEEE*, Zixuan Liu, Lijian Wu, *Senior Member, IEEE*,
Teng Long, Yuzheng Chen, Xinru Li, Wucheng Ying, Boyang Shen, and Youtong Fang, *Senior Member, IEEE*

***Abstract*-- This paper analyzed and compared the complex permeance model (CPM) and nonlinear analytical model (NAM) for surface-mounted permanent magnet (SPM) motor using voltage source inverter (VSI). For linear CPM, the slotting effect is represented using the improved complex permeance function that describes the real slot shape rather than infinitely deep slot. NAM is extended from CPM and it replaces the magnetic potential drop of stator iron by the equivalent virtual current in the slot-opening and tooth-tip to account for nonlinearity effect. The nonlinear inductance of SPM motor including the main phase inductance, slot leakage inductance, tooth-tip leakage inductance, and end winding leakage inductance is calculated using the frozen permeability method, which is the key to solve the electric circuit with VSI. The instantaneous back-EMF is calculated from the nonlinear back-EMF coefficient and the back-EMF neglecting iron nonlinearity. The electromagnetic torque obtained from motor model is used in the mechanical model and then the rotational speed and rotor position are obtained for the electric circuit model. Hence, the iterative solving process for the motor system is established to calculate the transient performance of SPM motor using VSI. Compared with CPM, NAM can greatly improve the calculation accuracy, which is also validated by both FEM and experiment. Besides, the proposed NAM is computationally efficient, which is useful for both motor design and motor control.**

***Index Terms*—analytical model, voltage source inverter, iron nonlinearity, complex permeance model.**

I. Introduction

PERMANENT magnet (PM) motors have drawn great attention due to the high efficiency and simple structure. For the PMSM, both design method and control strategy play an important part in improving the electromagnetic performance to the greatest extend. However, most researches focus on the motor design or motor control separately to reduce the computational time and therefore the motor systems will lose some advantage in the real applications. Thus, cosimulation receive massive attention for the whole system design [1]-[16].

For analyzing the PM motor with external circuit, the nonlinear winding inductance and back-EMF should be extracted from the motor model first. There are three methods to build the motor model: numerical method, circuit-based method, and analytical method. For the numerical method, finite-element model (FEM) can accurately consider the nonlinearity and complex geometry of the PM motors and it is capable to predict the electromagnetic performance of most PM motors accurately. The cosimulation combining FEM software with circuit simulation software was proposed for linear induction motor [2], synchronous reluctance motor [3], brushless direct-current (BLDC) motor [4]-[5], doubly salient PM motor [6], PM synchronous motor [7]-[8], etc. Although the FEM coupled with external circuit can be instantaneously solved in the cosimulation, its high prediction accuracy will accompany with large computational burden, making it unpractical for motor optimization. To overcome this disadvantage, offline calculation of FEM is often performed to establish the nonlinear motor model in the electric circuit simulation. The electromagnetic features of the motor are extracted from FEM results and they are represented using the looking up table [9]-[11] or nonlinear function [12]-[16]. Hence, only little computational resource is required for analyzing the transient characteristic of the motor coupled with electric circuit. However, the motor models from offline FEM calculation are still different from the real-time characteristic of real motors.

For the circuit-based method, magnetic circuit model (MCM) is proposed to analyze the nonlinearity of electric motors but its accuracy and computational speed is significantly influenced by the size of magnetic circuit matrix [17]-[18]. Fleming *et al.* provided a novel MCM for switched reluctance motor in the real-time emulation [19]. Fukuoka *et al.* introduced reluctance network for planetary-type magnetic gear and then performed transient analyses at different loads [20]. Cao *et al.* optimized the SPM motor with equivalent magnetic network with high accuracy [21]. Mine *et al.* presented two simple techniques to speed up the solving process for magnetic reluctance in the induction machines and obtained their transient behavior with high accuracy [22]. Hence, the MCM (including reluctance network) can be a good substitute for FEM in the transient

This work was supported by the National Key R&D Program of China under Grant No. 2019YFE0123500, Zhejiang Provincial Natural Science Foundation of China under Grant No. LQ22E070003 and the Liaoning Provincial Natural Science Foundation of China under Grant No. 2021-KF-24-03. *(Corresponding author: Xiaoyan Huang).*

Zhaokai Li, Xiaoyan Huang, Zixuan Liu, Lijian Wu, and Youtong Fang are with Zhejiang University, Hangzhou, 310027, China.

Teng Long, Xinru Li, Wucheng Ying, and Boyang Shen are with Department of Engineering, University of Cambridge, Cambridge, CB2 1PZ, UK.

Yuzheng Chen is with Department of Electrical and Electronic Engineering, University of Nottingham, Nottingham NG7 2RD, U.K.

analysis of PM motors. Nevertheless, MCM shows poor performance to predict magnetic field with complex flux path, which leads to either low accuracy or huge computation.

The linear analytical model can only present the linear electromagnetic performance of PM motors [23]-[24]. It can be used to analyze the torque ripple of BLDC motors coupled with external circuit [25]. Xuan *et al.* proposed the winding function to obtain the inductance of fractional slot PM motors and then analyzed the three-phase short circuit current [26]. However, these analytical models are not suitable for cosimulation since they cannot improve the calculation accuracy due to their linear property. To solve this problem, the nonlinear analytical models were proposed in [27]-[31] and the equivalent current was introduced to represent iron nonlinearity. However, these models have been verified using current source at steady-state condition and there is lack of research about the nonlinear analytical models with voltage source inverter.

This paper investigates a nonlinear analytical model (NAM) for predicting the transient performance of SPM motor using voltage source inverter (VSI). The back-EMF, inductance, and torque considering both slotting effect and nonlinearity effect are extracted from the NAM using the nonlinearity factor. Coupled with electric circuit model and mechanical model, the transient performance of SPM motor using VSI considering PWM effect can be obtained with great calculation accuracy and high calculation efficiency. The differences between CPM and NAM are compared and investigated to show the improvement for motor control simulation, where the constant and linear parameters are usually preferred to represent the nonlinear motor and therefore introduce large errors. Finally, FEM cosimulation and experiment are carried out to verify the proposed model.

The paper is structured as follows: Section I summarizes the recent research about the motor model which requires high calculation accuracy and high calculation efficiency. Under the circumstance, the nonlinear analytical model can be the perfect candidate for analyzing the transient performance of SPM motor using VSI. In Section II, the NAM which combined MCM and CPM is proposed to predict the magnetic field distribution of SPM motor. Then, the electric circuit model transforms the magnetic field from NAM into the circuit component to obtain the next phase current. The mechanical model is used to calculate the next rotor position based on the predicted torque using NAM. Their coupling is essential to obtain the transient performance of SPM motor. Section III analyzed the transient performance of a 15-slot/4-pole prototype motor at constant speed and at constant torque using CPM, NAM, FEM and experiment. They all verifies the high calculation accuracy and efficiency of NAM. Finally, the conclusion is draw in Section IV.

II. Analytical Model with Voltage Source Inverter

The analytical model with voltage inverter consists of three parts: magnetic model, electric circuit model, and mechanical model. In the motor model, iron nonlinearity is represented by the equivalent current in the slot-opening and tooth-tip. Hence, the analytical air-gap field of SPM motor can be directly obtained. In the electric circuit model, the VSI with semiconductor devices is modelled according to the circuit theory while the nonlinear winding inductance and back-EMF is derived from the air-gap field of SPM motors. In the mechanical model, the motion state is obtained using the predicted torque from the nonlinear analytical model. By manipulating these mathematical models, the performance of SPM motor will be iteratively obtained considering the nonlinearity effect and the influence of VSI.

A. Magnetic Model of SPM motor

To model the iron nonlinearity and slotting effect, the NAM combining MCM with CPM is proposed to calculate magnetic field of the whole motor. Fig. 1 gives the overall model to represent the SPM motor. The stator iron and slot region are replaced by the magnetic reluctance while the air-gap field is represented using the air-gap flux source. The rotor position only affects the value of air-gap flux source while the connection of magnetic reluctance in the MCM stays unchanged. The rotor permeability is assumed infinite because the rotor iron of SPM motor is usually thick enough to make the rotor flux density away from the saturation level for better performance [27]-[30].

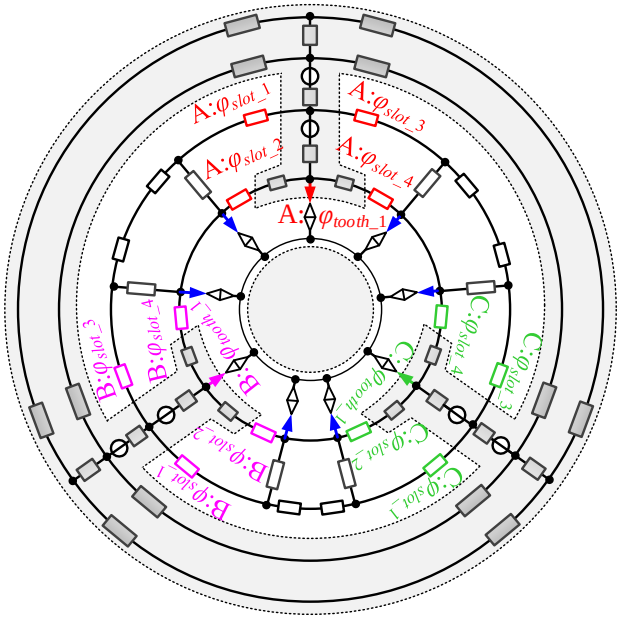

Fig. 1. The overall magnetic model for a three-slot SPM motor using NAM.

Based on Kirchhoff's laws, the mathematic solution of the MCM for SPM motor is represented as [28]

$$f(\mathbf{V}) = \mathbf{A}\boldsymbol{\Lambda}\mathbf{A}^{\mathrm{T}}\mathbf{V} - \mathbf{A}\boldsymbol{\Lambda}\mathbf{E} - \mathbf{A}\boldsymbol{\Phi} = 0 \tag{1}$$

where **A**, **Λ**, **V**, and **E** are the matrixes of the incidence, branch permeance, node magnetic potential, and branch MMF, respectively. **Φ** is the air-gap flux matrix, where **Φ**= [φ_{sk}, φ_{tk}, $\varphi_{s(k+1)}$, $\varphi_{t(k+1)}$ …]. The calculation flowchart of MCM is given in Fig. 2.

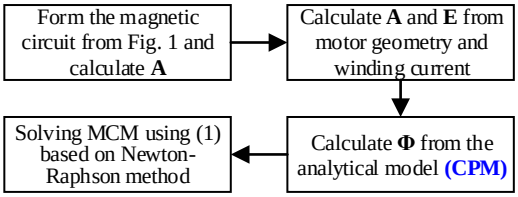

Fig. 2. The flowchart of calculating MCM.

In order to obtain the air-gap flux, the analytical model of slotted air-gap field is proposed using the improved complex permeance model rather than subdomain model to consider slotting effect and reduce the computational burden. Comparing with the subdomain model, the improved complex permeance model based on the conformal transformation can account for arbitrary groove type and tooth-tip with high accuracy. The complex permeance function is extracted from only one-slot region, which can reduce the calculation time while keeping the same high accuracy, as shown in the blue region of Fig. 3(a).

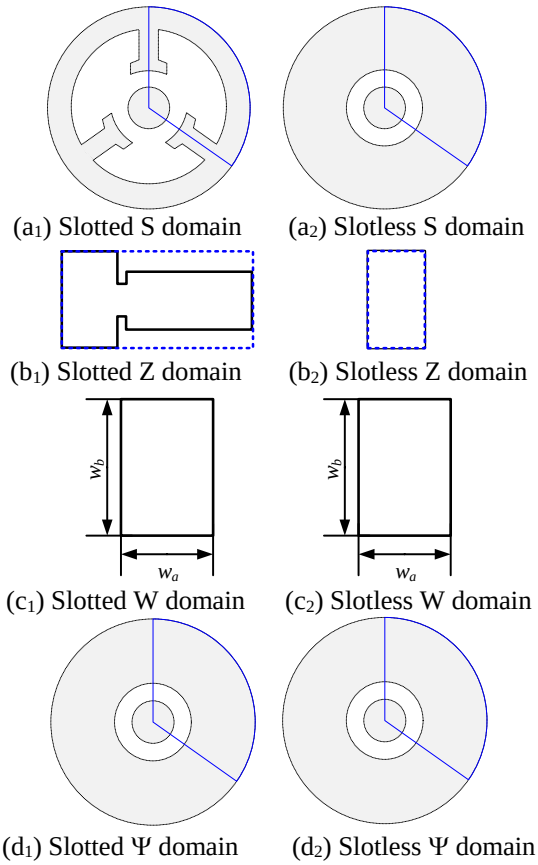

Fig. 3 The conformal transformations based on one-slot region.

Three conformal transformations are used to calculate the complex permeance function for both slotted and slotless air-gap region [32]

$$\frac{B_S}{B_\Psi}=\left(\frac{\partial\Psi}{\partial W}\right)^*\left(\frac{\partial W}{\partial Z}\right)^*\left(\frac{\partial Z}{\partial S}\right)^* \tag{2}$$

where

$$Z=\ln S \tag{3}$$

$$Z=g(W)=A_0\int\prod_{k=1}^{n-1}(W-w_k)^{-\frac{\alpha_k}{\pi}-1}dw+C_0 \tag{4}$$

$$\Psi=e^{-j\pi\left(\frac{2W-jw_b}{Q_s w_a}-1\right)} \tag{5}$$

where A_0, w_k, α_k, and C_0 are the Schwarz-Christoffel (SC) parameters and can be obtained from SC transformation. Q_s is the slot number.

As both slotted and slotless air-gap region will mapping to the same annulus in the Ψ domain of Fig. 3(d_1)-(d_2) using the same conformal transformations of (3)-(5), the improved complex permeance function which represents the relationship between slotted and slotless air-gap can be expressed as

$$\lambda=\left(\frac{B_{S\_slotted}}{B_{\Psi\_slotted}}\right)\Big/\left(\frac{B_{S\_slotless}}{B_{\Psi\_slotless}}\right)=\lambda_a+j\lambda_b \tag{6}$$

Thus, the radial and tangential component of slotted air-gap field can be obtained by

$$B_r=\lambda_a\left[B_{mr}+\sum_k B_{cr}(i_{sk})\right]+\lambda_b\left[B_{m\alpha}+\sum_k B_{c\alpha}(i_{sk})\right] \tag{7}$$

$$B_\alpha=\lambda_a\left[B_{m\alpha}+\sum_k B_{c\alpha}(i_{sk})\right]-\lambda_b\left[B_{mr}+\sum_k B_{cr}(i_{sk})\right] \tag{8}$$

where B_{mr}, $B_{m\alpha}$, B_{cr}, and $B_{c\alpha}$ are the radial and tangential component of slotless air-gap field produced by the PMs and the equivalent current including winding current and iron nonlinearity, respectively [28]. The equivalent current i_{sk} is calculated using

$$i_{sk}=-(V_{(k+1)}-V_k) \tag{9}$$

where V_k and $V_{(k+1)}$ are the adjacent magnetic potential.

Then, the air-gap flux source in Fig. 1, which is similar to the voltage controlled current source, is calculated by the integral of the air-gap flux density

$$\varphi_{ik}=l_{ef}r\int_{\alpha_{i1}}^{\alpha_{i2}}B_r(r,\alpha)d\alpha\ \text{, where } i=t,s \tag{10}$$

where l_{ef} is the active length of the motor. The calculation flowchart of the analytical model is given in Fig. 4. Finally, by solving (1) with the given rotor position and winding current, the magnetic field of SPM motor is obtained, which is essential to solve the electric circuit model and the mechanical model.

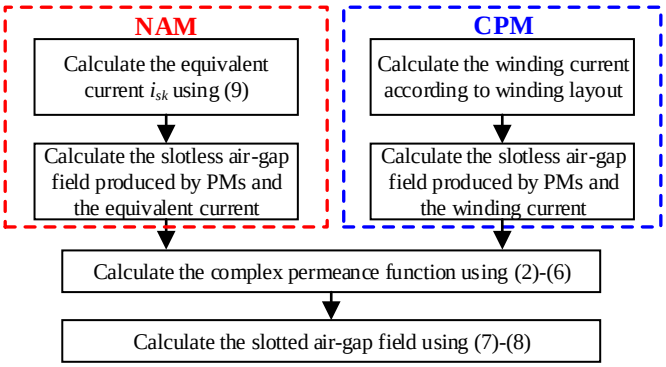

Fig. 4. The flowchart of calculating the air-gap field.

B. Electric Circuit Model

The electric circuit model is divided into two parts to obtain the transient performance of SPM motor, the control strategy and electric circuit. The control strategy, such as field-oriented control or direct torque control, gives the signal to the power semiconductor device in the voltage source inverter and therefore the winding current is produced in the electric circuit to drive the motor. In one switching cycle of power device, the output voltage is a PWM waveform generated by control

strategy and it is expressed in the Fourier form.

$$u_s(t) = m_p u_{s0} + \sum_{k=1}^{\infty} \frac{2u_{s0}}{\pi k} \sin\left(m_p k\pi\right) \cos(2\pi f_s kt + \alpha_{sk}) \quad (11)$$

where m_p, f_s and u_{p0} are the duty cycle, frequency and voltage value of PWM. α_{sk} represents the phase shift of the switching-on status.

In the electric circuit, the nonlinear inductance matrix $\mathbf{L_{ABC}}$, nonlinear back-EMF matrix $\mathbf{E_{ABC}}$, and resistance matrix $\mathbf{R_{ABC}}$ are used to represent the three-phase voltage $\mathbf{U_{ABC}}$ of SPM motor.

$$\mathbf{U_{ABC}} = \mathbf{L}\frac{d\mathbf{I_{ABC}}}{dt} + \mathbf{R_{ABC}}\mathbf{I_{ABC}} + \mathbf{E_{ABC}} \quad (12)$$

where $\mathbf{U_{ABC}} = \begin{bmatrix} u_A & u_B & u_C \end{bmatrix}^T$. $\mathbf{R_{ABC}} = \begin{bmatrix} R_A & R_B & R_C \end{bmatrix}^T$.

$\mathbf{I_{ABC}} = \begin{bmatrix} i_A & i_B & i_C \end{bmatrix}^T$. $\mathbf{E_{ABC}} = \begin{bmatrix} E_A & E_B & E_C \end{bmatrix}^T$.

$$\mathbf{L_{ABC}} = \begin{bmatrix} L_{AA} & M_{BA} & M_{CA} \\ M_{AB} & L_{BB} & M_{CB} \\ M_{AC} & M_{BC} & L_{CC} \end{bmatrix}.$$

It is noted that the calculation of inductance is not given in [27]-[30] and the back-EMF cannot be separated from the induced voltage. If the total induced voltage is used to solve the electric circuit model instead of the nonlinear inductance and back-EMF, huge numerical errors will occur due to the iterative calculation of MCM in the magnetic model. Hence, this paper proposes a novel method to calculate the nonlinear inductance and back-EMF simultaneously based on the frozen permeability method. The phase flux linkages ψ_{ph} is calculated as

$$\psi_{ph} = N_c \sum_{i=1}^{\kappa} \left(\varphi_{tooth\_i} + \varphi_{slot\_i}\right) \quad (13)$$

where N_c is the number of turns in the coil. $ph \in$ [A,B,C]. φ_{tooth_i} and φ_{slot_i} are the air-gap flux flowing from tooth and slot based on NAM, as shown in Fig. 1. They are obtained from the flux distribution in the magnetic circuit according to the solution of Equation (1). Then, based on the winding layout of SPM motor, the phase flux linkage is extracted from the slot flux and air-gap flux for phase A, B, and C, as illustrated in Fig. 1. The corresponding induced voltage is the derivative of phase flux linkages. The calculation flowchart is shown in Fig. 5.

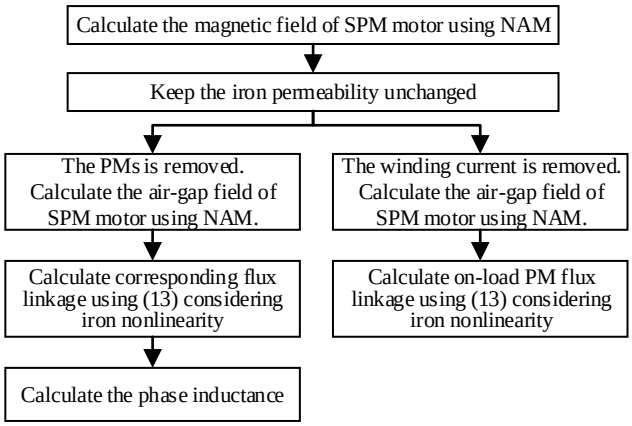

Fig. 5. The flowchart of frozen permeability method.

For the inductance calculation, the iron permeability is obtained from the magnetic model from (1) firstly and keeps unchanged at the same time. Then the air-gap flux produced by the equivalent current including winding current and iron nonlinearity is calculated using

$$B_r = \lambda_a \sum_k B_{cr}(i_{sk}) + \lambda_b \sum_k B_{c\alpha}(i_{sk}) \quad (14)$$

Therefore, the corresponding inductance L_{ph_m} is obtained by

$$L_{ph\_m} = \frac{\psi_{ph\_m}}{i_{ph\_w}} \quad (15)$$

where i_{ph_w} is the winding current. Ψ_{ph_m} is the corresponding phase flux linkages When the winding current is set as 1A to the magnetic model with unchanged iron permeability, L_{ph_m} can be obtained. Similarly, the mutual inductance can be calculated using (15).

The tooth-tip leakage inductance L_{ttl} is calculated using the leakage flux flowing in the air gap outside the slot-opening. When neglecting nonlinearity, it is expressed as [34]

$$L_{ttl} = \frac{12\mu_0}{Q_s} l_{ef} N_c^{\,2} \frac{1+g'}{2} \frac{5\delta}{5b_0 + 4\delta} \quad (16)$$

where δ is the air-gap length and b_0 is the width of slot-opening. g' represents average value of phase shift γ_k between different phase current in the kth slot, which is expressed as [34]

$$g' = \frac{1}{2q} \sum_{k=1}^{2q} \cos\gamma_k \quad (17)$$

where q is the number of slots per pole per phase. $\gamma_k = 60°$ if the coils in the kth slot belong to different phases or $\gamma_k = 0°$ if the coils in the kth slot belong to the same phase.

The nonlinearity factor for tooth-tip leakage flux c_L is defined as

$$c_L = \frac{L_{ph\_m}}{L_{ph\_inf}} \quad (18)$$

where both L_{ph_m} and L_{ph_inf} are calculated using (15) and their air-gap field is obtained using NAM and CPM neglecting PMs, respectively. Then, the phase flux linkage produced by the winding current can be predicted according to the winding layout and the corresponding inductance can be obtained, as shown in Fig. 5.

For the end winding leakage inductance L_{ew}, it is difficult to give an accurate analytical expression due to the complex geometry of end windings and the mutual influence of three-phase current. Hence, the empirical permeance factors are employed to determine the end winding leakage inductance, which is described in [34]. Thus, the total winding inductance can be obtained by

$$L_{ph} = L_{ph} + c_L L_{ttl} + L_{ew} \quad (19)$$

For the calculation of back-EMF considering nonlinearity effect, a nonlinear back-EMF coefficient c_{emf} is introduced to eliminate the numerical errors from the derivative of flux linkage to time

$$c_{emf} = \frac{\psi_{ph\_emf}}{\psi_{ph\_inf}} \quad (20)$$

where ψ_{ph_emf} and ψ_{ph_inf} are the on-load PM flux linkage for SPM motor from the NAM and CPM, respectively. Both of them are calculated when neglecting winding current. Then the

phase flux linkage produced by the PMs only can be predicted according to the winding layout for ψ_{ph_inf}. As for ψ_{ph_emf}, the air-gap field produced by the PMs and the equivalent nonlinearity current is calculated according to Fig. 1, when the iron permeability stays finite and unchanged to account for iron nonlinearity using the frozen permeability method. The calculation flowchart is shown in Fig. 5. It is noted that the proposed coefficients c_L and c_{emf} are also promising for other types of motors such as IPM motors and vernier PM motors, which will be investigated in the future. The criterion of back-EMF is obtained from the derivative of the open-circuit flux linkage to time

$$E_{ph\_inf}(t)=\frac{d\psi_{ph\_inf}}{dt}=\sum_{k=1}^{\infty}kpw_r\psi_{pk}\cos(kpw_rt+\theta_{ek}) \quad (21)$$

where w_r is the rotational angular speed. p is the pole pairs. ψ_{pk} and θ_{ek} are the k^{th} harmonic amplitude and phase of flux linkage in one phase. Hence, the back-EMF under on-load condition considering nonlinearity effect is calculated by

$$E_{ph}(t)=c_{emf}E_{ph\_inf}=\sum_{k=1}^{\infty}kpw_rc_{emf}\psi_{pk}\cos(kpw_rt+\theta_{ek}) \quad (22)$$

For the electric circuit of conventional inverter in Fig. 6(a), the general circuit equation for three phase of SPM motor can be obtained according to Kirchhoff law.

$$\begin{cases}s_Au_A(t)+s_Bu_B(t)+s_Cu_C(t)=u_s(t)\\ i_A(t)+i_B(t)+i_C(t)=0\end{cases} \quad (23)$$

where s_A, s_B and s_C represent the switching status of three phase fully controlled bridge. s_A, s_B, $s_C\in$ [-1,0,1]. The analytical solution of phase current can be obtained as

$$i_{ph}(t)=i_{ph0}+i_{pht}e^{-\frac{t}{\tau_{ph}}}+\sum_{k=1}^{\infty}i_{phkc}\cos(pw_rkt)+i_{phks}\sin(pw_rkt) \quad (24)$$

where $ph\in$[A,B,C].

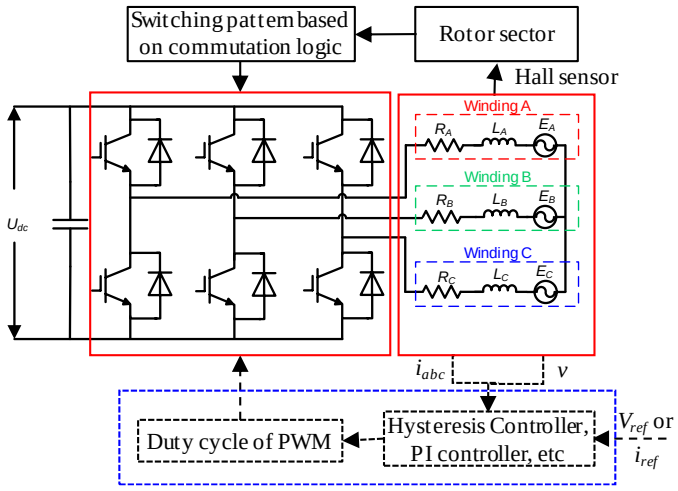

Fig. 6. The electric circuit and control strategy of the BLDC motor system.

For BLDC SPM motor, the trapezoidal control technique is used to produce constant torque, Fig. 6. In fact, the control strategy including hysteresis control or PI control has already been widely used in the industrial application for BLDC motor system, which can be directly utilized with NAM. To focus on the effectiveness of the proposed model, the control strategy is simplified, in which the duty cycle of PWM is set as constant.

In the electric circuit, there are two general states: one is two-phase-current mode at steady-state condition and the other is three-phase-current mode at commutation condition. When the current is only in phase *A* and *C* at steady-state condition, the corresponding value of phase *A* in (24) can be obtained as

$$\begin{aligned}i_{At}&=i_{tA0}-\frac{u_{s0}}{z_1}-\sum_{k=1}^{\infty}i_{Akc}\\ i_{Akc}&=-\frac{\sqrt{3}kpw_rc_{emf}\psi_{Ak}}{z_1^2+z_2^2}\left[z_1\cos(\theta_{Aek}+\frac{\pi}{6})-z_2\sin(\theta_{Aek}+\frac{\pi}{6})\right]\end{aligned} \quad (25)$$

where i_{tA0} is the initial current of phase A.

$z_1=R_A+R_C$.

$z_2=\left(L_A+M_{CA}+L_C+M_{AC}\right)kpw_r$.

$\tau_A=\dfrac{L_A+M_{CA}+L_C+M_{AC}}{R_A+R_C}$.

When there is commutation from phase B to phase C at commutation condition, the corresponding winding current in (24) can be obtained as

$$\begin{aligned}i_{At}&=i_{tA0}+\frac{R_B}{z_1}u_{s0}-\sum_{k=1}^{\infty}i_{Akc}\\ i_{Bt}&=i_{tB0}-\frac{R_A}{z_1}u_{s0}-\sum_{k=1}^{\infty}i_{Bkc}\\ i_{Ct}&=-i_{At}-i_{Bt}\\ \mathbf{I_k}&=\mathbf{Z_k^{-1}}*\mathbf{U_k}\end{aligned} \quad (26)$$

where i_{tB0} is the initial current of phase B.

$\tau_A=\dfrac{L_A}{R_A}$.

$\tau_B=\dfrac{L_B}{R_B}$.

$z_3=R_AR_C+R_AR_B+R_CR_B$.

$\mathbf{I_k}=\left[i_{Akc}\quad i_{Aks}\quad i_{Bkc}\quad i_{Bks}\right]^{\mathrm{T}}$.

$$\mathbf{Z_k}=\begin{bmatrix}L_Bkpw_r & R_B & L_Ckpw_r & -R_C\\ R_B & L_Bkpw_r & -R_C & -L_Ckpw_r\\ R_A & L_Akpw_r & R_A+R_C & (L_A+L_C)kpw_r\\ L_Apw_rk & -R_A & (L_A+L_C)kpw_r & -\left(R_A+R_C\right)\end{bmatrix}$$

$$\mathbf{U_k}=\sqrt{3}kpw_rc_{emf}\psi_A\left[\cos(\theta_{ek})\quad \sin(\theta_{ek})\quad \cos(\theta_{ek}+\frac{\pi}{6})\quad \sin(\theta_{ek}+\frac{\pi}{6})\right]^{\mathrm{T}}$$

It is noted that the similar expression of other phase current under either steady-state condition or commutation condition can be accordingly obtained using (23)-(24). It is important to choose the proper time interval for obtaining the accurate winding current in the calculation, as the rotor speed is regard as constant during the time interval.

C. Mechanical Model

According to Maxwell tensor theory, the torque calculation of the SPM motor is expressed as

$$T_e=\frac{1}{\mu_0}l_{ef}r^2\int_0^{2\pi}B_rB_\alpha d\alpha \quad (27)$$

Based on the rotational equation, the mechanical model is expressed as

$$T_e - T_{load} = J_0\beta + Bw_r \tag{28}$$

where β represents the angular acceleration. T_{load} represents the load torque. B is the coefficient of viscosity. Hence, the rotor speed and position can be numerically obtained. Accordingly, the drive signal of VSI in the external electric circuit is determined to solve the phase current.

In order to simplify the mutual influence between the torque and current in the external circuit, the torque coefficient c_t which represents nonlinearity effect on the torque value is introduced to replace the complicated torque equation (27)

$$c_t = \frac{T_{e\_non}}{T_{e\_inf}} \tag{29}$$

where T_{e_non} is obtained using NAM considering nonlinearity effect and T_{e_inf} is predicted using CPM neglecting iron nonlinearity. It is note that the torque coefficient c_t will be redetermined at the beginning of every time interval and stays unchanged during the corresponding time interval to calculate the next rotor position for both magnetic model and electric circuit model.

D. Solving Process

As shown in Fig. 7, the solving process of NAM combines magnetic model, electric circuit model, and mechanical model in series to obtain the winding current. There are two iterative loops in the solving process. The outer loop obtains three phase current in electric circuit model and determined the rotor position in the mechanical model while the inner loop gives the air-gap flux flowing to the stator of the SPM motor considering nonlinearity effect. As for CPM, the linear analytical model is used to directly obtain the phase inductance and therefore only one solving loop is used for predicting the circuit current and torque. Compared with the FEM cosimulation, the NAM significantly decreases its calculation in the magnetic model due to the reduced node in the MCM and the simplified air-gap field model using CPM. Besides, as the iron nonlinearity is represented by equivalent nonlinearity current, the NAM will achieve higher accuracy of motor performance than CPM.

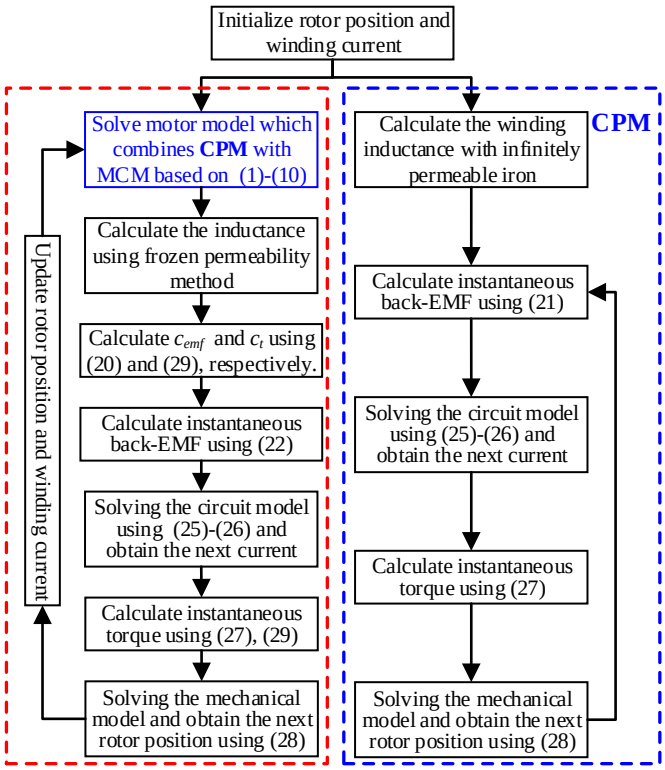

Fig. 7. The flowchart of calculating the NAM and CPM.

III. FE Calculation and Experiment Validation

A 15-slot/4-pole SPM motor was built to verify the proposed models under VSI, as shown in Fig. 8. The motor was driven by VSI using trapezoidal control technique in Fig. 9. Its main parameters are given in TABLE I. In the three-phase full-bridge inverter of Fig. 3, DC voltage supply is 20V. The typical forward voltage of the IGBT is 1.5V from the datasheet.

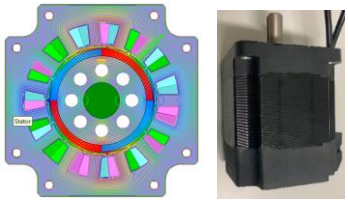

(a) (b)

Fig. 8. The 15-slot/4-pole SPM motor: (a) FE model and (b) prototype machine.

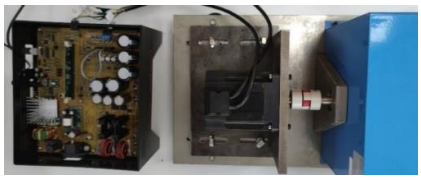

Fig. 9. The experimental setup of SPM motor.

TABLE I
THE MAIN PARAMETERS OF PROTOTYPE SPM MOTOR

Parameter	Value
Stator outer length	86mm
Stator outer radius	48mm
Slot-opening	1.5mm
Tooth body width	5mm
Magnet thickness	3mm
Pole-arc to pole-pitch ratio	1

Rotor outer radius	20mm
Shaft radius	8mm
Active length	55mm
Number of parallel branches	11

To analytically calculate the transient characteristic of SPM motor, the open-circuit back-EMF is required to obtain the on-load nonlinear back-EMF while reducing the errors of numerical calculation. Fig. 10 gives the waveforms of back-EMF using CPM, NAM, FEM, and from experiment. It can be seen that both CPM and linear FEM calculation predict slightly higher fundamental harmonic back-EMF than NAM and nonlinear FEM results, which shows that NAM has higher accuracy than CPM.

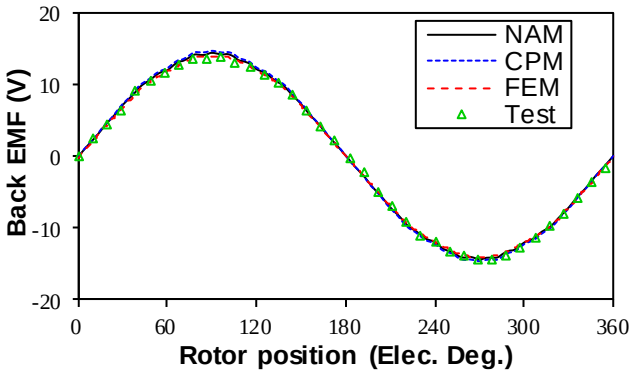

Fig. 10. The comparison of back-EMF waveforms using HFM, CPM, and FEM and from experiment at 1000rpm.

When the SPM motor is operated at the constant speed of 800rpm with duty cycle of 0.8 and switching frequency (f_s) of 1kHz in the external circuit using trapezoidal control technique, its transient characteristic can be obtained using CPM, NAM, and FEM to investigate the influence of VSI on the motor performance. Fig. 11 illustrates that the NAM prediction of current waveform agrees well with FEM calculation but CPM underestimates the current value at constant speed. The larger errors of CPM prediction come from the overestimated back-EMF amplitude and inductance using CPM due to neglecting the nonlinearity effect of SPM motor compared with NAM and FEM at the same rotational speed. Therefore, the induced voltage of SPM motor predicted using CPM is larger than that using NAM or FEM. With the same phase resistance and voltage source inverter, CPM will underestimate the current value. Similar observation can be found in the torque waveform of Fig. 12. As for the line voltage waveform of Fig. 13, both CPM and NAM has high accuracy, which means that the iron nonlinearity has small influence on the on-load back-EMF.

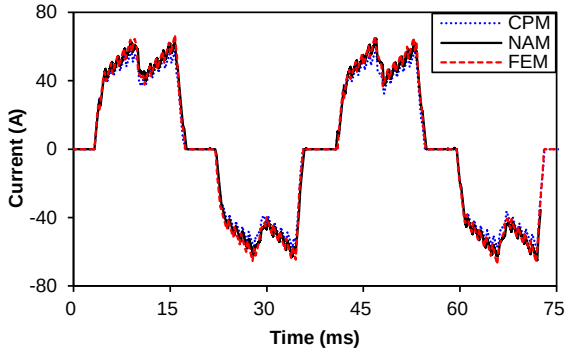

Fig. 11 The current waveform of SPM motor at 800rpm.

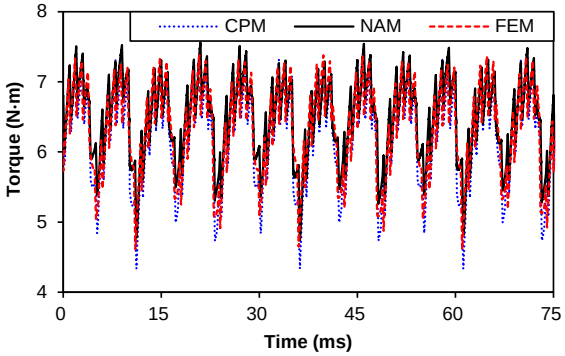

Fig. 12 The torque waveform of SPM motor at 800rpm.

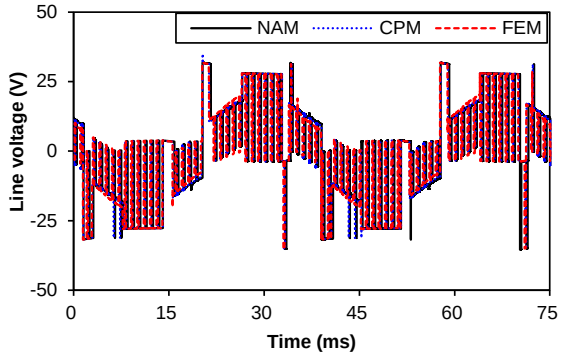

Fig. 13 The line voltage of SPM motor at 800rpm.

Then, the SPM motor is operated at constant torque from stationary condition. The external circuit is driven according to the rotor position from hall sensor with duty cycle of 0.8 and switching frequency (f_s) of 10kHz. From the comparison of phase inductance in Fig. 14, NAM prediction is closer to FEM results than CPM in both self-inductance and mutual-inductance, which improves the accuracy of the proposed model for transient analysis. The start-up speed of Fig. 15 shows that the NAM can accurately follow the speed of FEM calculation while CPM has static error at constant torque of 1N·m due to the large errors of back-EMF and inductance. In Fig. 16, both CPM and NAM can accurately predict the initial voltage amplitude, but CPM shows low accuracy in predicting the phase and frequency of voltage. In Figs. 17-18, the predicted current and torque using NAM agree well with FEM results. As for CPM, large errors are observed in the phase and frequency for both current and torque at start-up.

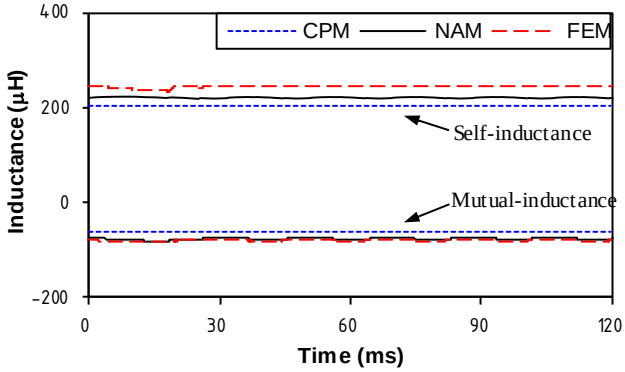

Fig. 14 The phase inductance of SPM motor at start-up with duty cycle of 0.8 and constant torque of 1N·m.

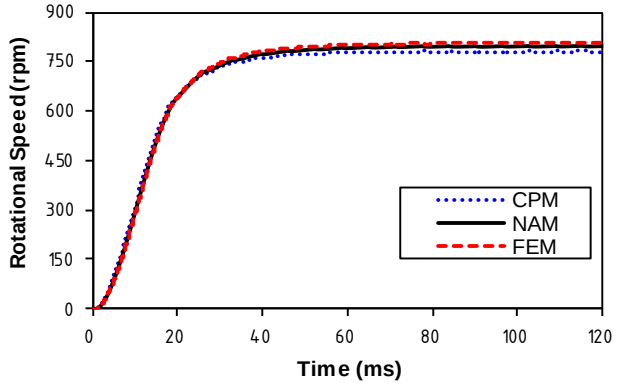

Fig. 15. The start-up speed of SPM motor with duty cycle of 0.8 and constant torque of 1N·m.

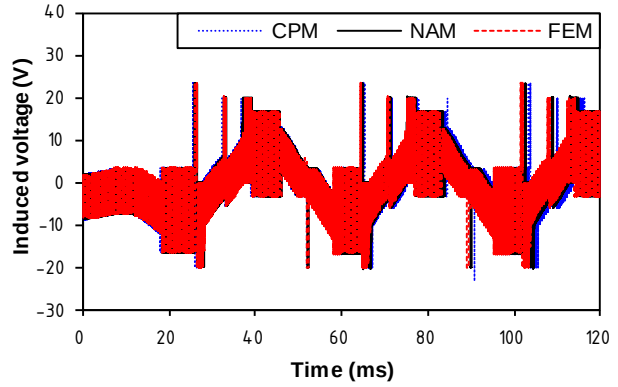

Fig. 16. The line voltage waveform of SPM motor at start-up with duty cycle of 0.8 and constant torque of 1N·m.

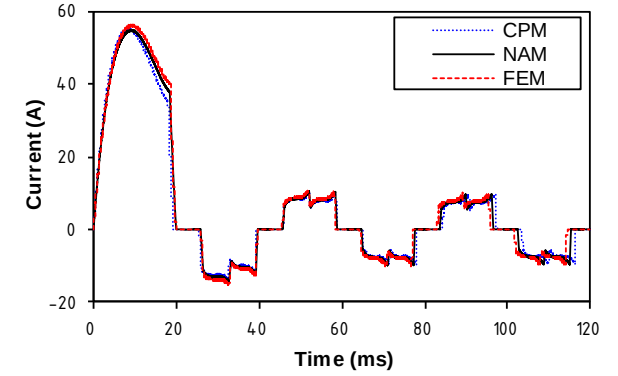

Fig. 17. The current waveform of SPM motor at start-up with duty cycle of 0.8 and constant torque of 1N·m.

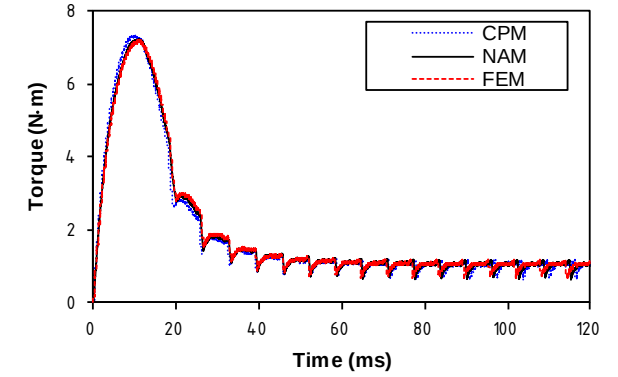

Fig. 18. The torque waveform of SPM motor at start-up with duty cycle of 0.8 and constant torque of 1N·m.

When the SPM motor reached steady state at duty cycle of 0.8 and constant torque of 1N·m, the harmonic line voltage and current waveform are predicted using CPM, NAM, and FEM. Their accuracy is validated by experimental results, as shown in Figs. 19-20. It can be seen that NAM and FEM can predict more accurate voltage and current than CPM predictions. In Fig. 21, CPM has similar torque value to FEM result but underestimates the torque frequency while NAM agrees well with FEM result. Figs. 22-23 show the variation of steady speed of SPM motor to the DC voltage and duty cycle at constant torque of 1N·m and switching frequency of 10kHz. Comparing with experimental results, both NAM and FEM shows great accuracy for predicting the steady speed using VSI. The motor speed has negligible influence on the prediction accuracy of the proposed model.

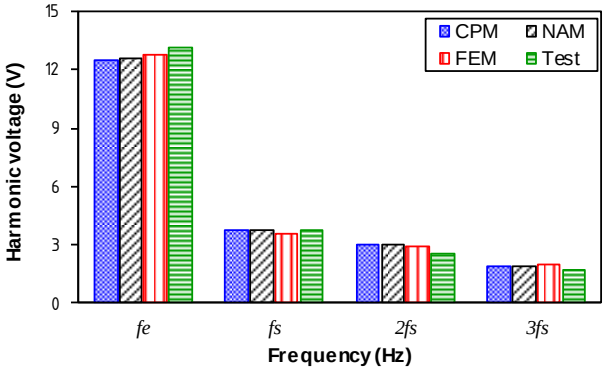

Fig. 19. The steady state of induced voltage waveform in the SPM motor with duty cycle of 0.8 and constant torque of 1N·m.

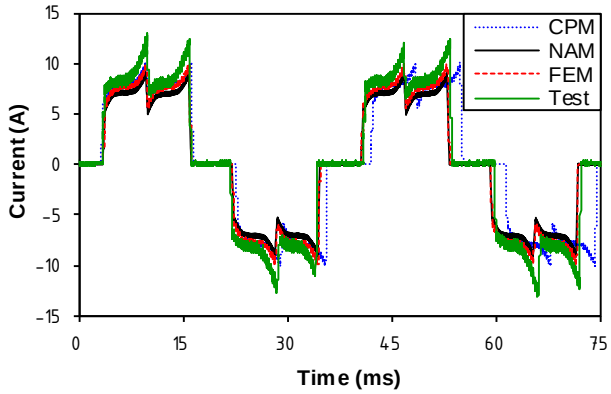

Fig. 20. The steady state of current waveform in the SPM motor with duty cycle of 0.8 and constant torque of 1N·m.

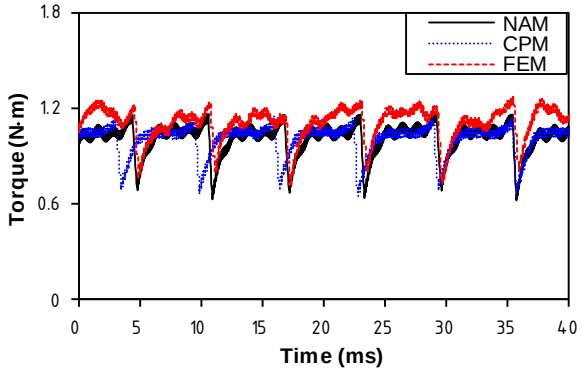

Fig. 21. The steady state of torque waveform in the SPM motor with duty cycle of 0.8 and constant torque of 1N·m.

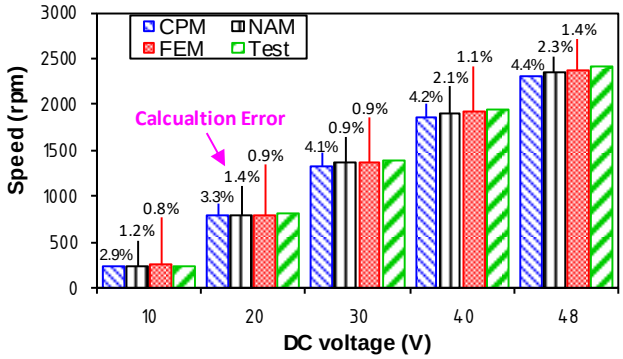

Fig. 22. The variation of steady speed to DC voltage for SPM motor with duty cycle of 0.8 and constant torque of 1N·m.

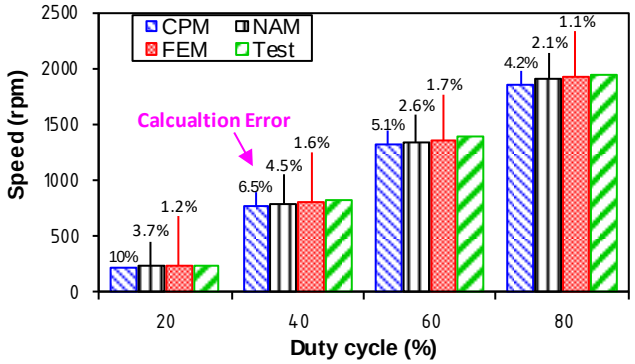

Fig. 23. The variation of steady speed to DC voltage for SPM motor with DC voltage of 40V and constant torque of 1N·m.

As for the calculation resource, the main simulation parameters are listed in TABLE II to make a fair comparison. The FEM is running in the Ansys Maxwell platform while CPM and NAM are executed in MATLAB. The total mesh node using FEM is significantly larger than the magnetic circuit node of NAM, which reflects the computational complexity in solving the magnetic model. The calculation time of CPM, NAM, and FEM is given in TABLE III. It can be seen that FEM consumes the largest calculation resource to predict transient characteristic of SPM motor at either constant speed or constant torque condition while CPM takes the least computational time under the same work condition. Since the calculation of magnetic reluctance or finite element consumes most of the solving time, the node number is the key factor to affect calculation time. The NAM can save nearly 1/20 computational time of FEM while keeping high accuracy. Besides, the increase of carrier frequency will directly raise the computational burden, as shown in TABLE III. To guarantee the same calculation accuracy, it is required to give the shorter time interval and increase the calculation step in the analytical models, therefore leading to consuming longer calculation time. Thus, the proposed NAM will show significant advantage over FEM in calculation efficiency, since high switching frequency is always preferred in the advanced motor system.

TABLE II
SIMULATION PARAMETERS FOR SPM MOTOR

Model	Air-gap tangential segment*	Total Node	Simulation time
CPM		0	
NAM	360	255	120ms
FEM		12134	

*The division of the circular air-gap path to show flux density distribution

TABLE III
SOLVING TIME OF CPM, NAM AND FEM FOR SPM MOTOR

Mode / Model	Constant speed (f_s=1kHz)	Constant torque (f_s=10kHz)
CPM	254s	1643s
NAM	449s	2334s
FEM	10588s	478583s

IV. CONCLUSION

This paper proposed the CPM and NAM to account for slotting effect for the transient analysis of SPM motor using VSI and therefore investigated the effectiveness of analytical models coupled with external circuit. In NAM, the nonlinear phase inductance and back-EMF can be obtained analytically to replace the SPM motor in the drive circuit. To solve the NAM, two iterative loops are required to combine the magnetic model with electric circuit model and mechanical model. Hence, the transient performance of the SPM motor can be obtained using VSI. Compared with CPM, NAM has high accuracy to predict the electromagnetic performance of SPM motor at constant speed or constant torque in the motor system. Besides, it saves more than 95% of computational time using FEM.

REFERENCES

[1] Zhaokai Li, Yuzheng Chen, Xiaoyan Huang, Xinru Li, Wucheng Ying, Boyang Shen, Lijian Wu, Youtong Fang, and Teng Long, "Dynamic modeling of surface-mounted permanent magnet motors considering saturation," in *ECCE 2019.*, Sep. 2019, pp. 5624–5628.

[2] Byung-II Kwon, Kyung-II Woo, and Sol Kim, "Finite element analysis of direct thrust-controlled linear induction motor," *IEEE Trans. Magn.*, vol. 35, no. 3, pp. 1306-1309, May 1999.

[3] F. Parasiliti, M. Villani and A. Tassi, "Dynamic analysis of synchronous reluctance motor drives based on Simulink® and finite element model," in *Proc. IECON 2006.*, 2006, pp. 1516-1520.

[4] M. Fasil, N. Mijatovic, B. B. Jensen and J. Holboll, "Nonlinear dynamic model of PMBLDC motor considering core losses," *IEEE Trans. Ind. Electron.*, vol. 64, no. 12, pp. 9282-9290, Dec. 2017.

[5] O. A. Mohammed, S. Liu, and Z. Liu, "A phase variable model of brushless DC motors based on finite element analysis and its coupling with external circuits," *IEEE Trans. Magn.*, vol. 41, no. 5, pp. 1576-1579, May 2005.

[6] W. Zhao, M. Cheng, X. Zhu, W. Hua, and X. Kong, “Analysis of fault-tolerant performance of a doubly salient permanent-magnet motor drive using transient cosimulation method,” *IEEE Trans. Ind. Electron.*, vol. 55, no. 4, pp. 1739–1748, Apr. 2008.

[7] L. Di Leonardo, F. Parasiliti, M. Tursini and M. Villani, "Transient analysis of PM synchronous motor drives by finite element model co-simulation," in *Proc. IECON 2013*., 2013, pp. 6834-6840.

[8] M. A. Jabbar, Zhejie Liu and Jing Dong, "Time-stepping finite-element analysis for the dynamic performance of a permanent magnet synchronous motor," *IEEE Trans. Magn.*, vol. 39, no. 5, pp. 2621-2623, Sept. 2003.

[9] L. Quéval and H. Ohsaki, "Nonlinear abc-model for electrical machines using N-D lookup tables," *IEEE Trans. Energy Convers.*, vol. 30, no. 1, pp. 316-322, March 2015.

[10] J. Wu, J. Wang, C. Gan, Q. Sun and W. Kong, "Efficiency optimization of PMSM drives using field-circuit coupled FEM for EV/HEV applications," *IEEE Access*, vol. 6, pp. 15192-15201, 2018.

[11] T. N. Matzen and P. O. Rasmussen, "Modelling magnetic saturation effects in IPMSMs for use in sensorless saliency based methods," in *Proc. 2007 ECPEA*, 2007, pp. 1-8.

[12] Y. Kano, K. Watanabe, T. Kosaka and N. Matsui, "A novel approach for circuit-field-coupled time-stepping electromagnetic analysis of saturated interior PM motors," I*EEE Trans. Ind. Appl.*, vol. 45, no. 4, pp. 1325-1333, July-Aug. 2009.

[13] M. Fazil and K. R. Rajagopal, "Nonlinear dynamic modeling of a single-phase permanent-magnet brushless DC motor using 2-D static finite-element results," *IEEE Trans. Magn.*, vol. 47, no. 4, pp. 781-786, April 2011.

[14] G. Luo, R. Zhang, Z. Chen, W. Tu, S. Zhang, and R. Kennel, “A novel nonlinear modeling method for permanent-magnet synchronous motors,” *IEEE Trans. Ind. Electron.*, vol. 63, no. 10, pp. 6490–6498, Oct. 2016.

[15] W. Liang, J. Wang, T. Lu and W. Fang, "A new method for multiple finite-element models in cosimulation with electrical circuit using machine multiloop modeling scheme," *IEEE Trans. Ind. Electron.*, vol. 61, no. 12, pp. 6583-6590, Dec. 2014.

[16] M. Tursini, M. Villani, A. Di Tullio, G. Fabri, and F. P. Collazzo, “Nonlinear model suitable for the offline cosimulation of fault-tolerant PM motors drives,” *IEEE Trans. on Ind. Appl.*, vol. 53, no. 4, pp. 3719–3729, Jul. 2017.

[17] X. Huang, M. Zhu, W. Chen, J. Zhang and Y. Fang, "Dynamic reluctance mesh modeling and losses evaluation of permanent magnet traction motor," *IEEE Trans. Magn.*, vol. 53, no. 6, pp. 1-4, June 2017.

[18] F. Chai, L. Gan, and Y. Yu, “Magnetic field analysis of an iron-cored tiered type permanent magnet spherical motor using modified dynamic reluctance mesh method,” *IEEE Trans. Ind. Electron.*, vol. 67, no. 8, pp. 6742–6751, Aug. 2020.

[19] F. E. Fleming and C. S. Edrington, "Real-time emulation of switched reluctance machines via magnetic equivalent circuits," *IEEE Trans. Ind. Electron.*, vol. 63, no. 6, pp. 3366-3376, June 2016.

[20] M. Fukuoka, K. Nakamura and O. Ichinokura, "Dynamic analysis of planetary-type magnetic gear based on reluctance network analysis," *IEEE Trans. Magn.*, vol. 47, no. 10, pp. 2414-2417, Oct. 2011.

[21] D. Cao, W. Zhao, J. Ji, and Y. Wang, “Parametric equivalent magnetic network modeling approach for multi-objective optimization of PM machine,” *IEEE Trans. Ind. Electron.*, vol. 68, no. 8, pp. 6619-6629, 2021.

[22] L. Mine, S. Goyal and A. A. E. Abdallh, "Improved dynamic modeling of squirrel-cage induction machines using magnetic reluctance network theory," in *Proc. ICEMS 2018*, 2018, pp. 555-559.

[23] V. Z. Faradonbeh, A. Rahideh, M. M. Ghahfarokhi, E. Amiri, A. D. Aliabad, and G. A. Markadeh, “Analytical Modeling of Slotted, Surface-Mounted Permanent Magnet Synchronous Motors With Different Rotor Frames and Magnet Shapes,” *IEEE Trans. Magn.*, vol. 57, no. 1, pp. 1–13, Jan. 2021.

[24] S. G. Min and B. Sarlioglu, “Analytical prediction and multiconstrained nonlinear optimization of slotted linear PM motors taking into account two-dimensional end effects,” *IEEE Trans. Ind. Electron.*, vol. 67, no. 4, pp. 2965–2976, Apr. 2020.

[25] X. Wang, Q. Li, S. Wang and Q. Li, "Analytical calculation of air-gap magnetic field distribution and instantaneous characteristics of brushless DC motors," *IEEE Trans. Energy Convers.*, vol. 18, no. 3, pp. 424-432, Sept. 2003.

[26] H. V. Xuan, H. Polinder, D. Lahaye, and J. A. Ferreira, "Modeling for the design of fractional slot PM machines with concentrated windings protected from demagnetization during three-phase short circuit," in *Proc. ECCE 2012*, 2012, pp. 1276-1283.

[27] L.J. Wu, Z. Li, X. Huang, Y. Zhong, Y. Fang and Z.Q. Zhu, "A hybrid field model for open-circuit field prediction in surface-mounted PM machines considering saturation," *IEEE Trans. Magn.*, vol. 54, no. 6, pp. 1-12, 2018.

[28] L.J. Wu, Z. Li, D. Wang, H. Yin, X. Huang and Z.Q. Zhu, "On-load field prediction of surface-mounted PM machines considering nonlinearity based on hybrid field model," *IEEE Trans. Magn.*, vol. 55, no. 3, pp. 1-11, 2019.

[29] L. Wu, H. Yin, D. Wang and Y. Fang, "A nonlinear subdomain and magnetic circuit hybrid model for open-circuit field prediction in surface-mounted PM machines," *IEEE Trans. Energy Convers.*, vol. 34, no. 3, pp. 1485-1495, 2019.

[30] L. Wu, H. Yin, D. Wang, and Y. Fang, "On-load field prediction in SPM machines by a subdomain and magnetic circuit hybrid model," *IEEE Trans. Ind. Electron.*, vol. 67, no. 9, pp. 7190-7201, Sept. 2020.

[31] S. Li, W. Tong, M. Hou, S. Wu and R. Tang, "Analytical model for no-load electromagnetic performance prediction of V-shape IPM motors considering nonlinearity of magnetic bridges," *IEEE Trans. Energy Convers.*, in press.

[32] K. Boughrara, R. Ibtiouen, D. Zarko, O. Touhami, and A. Rezzoug, “Magnetic field analysis of external rotor permanent-magnet synchronous motors using conformal mapping,” *IEEE Trans. Magn.*, vol. 46, no. 9, pp. 3684–3693, Sep. 2010.

[33] V. Ostovic, *Dynamics of saturated electric machines*. New York, NY, USA: Springer-Verlag, 1989.

[34] J. Pyrhönen, T. Jokinen, and V. Hrabovcová, *Design of Rotating Electrical Machines.* Chichester, West Sussex, UK: Wiley, 2008, pp. 225-253.